Bulletin of Geophysics and Oceanography Vol. 67, n. 3, pp. 527-546; September 2026
DOI 10.4430/bgo00526

Relationship between satellite-based tectonic lineament-surface temperature and antimony and iron mineralisation on the southern margin of the Nigde Massif (central Anatolia, Turkey)

R. Demircioğlu[1] and E. Kaya[2]

[1] *Department of Emergency Aid and Disaster Management, Aksaray University, Aksaray, Turkey*
[2] *Map and Cadastre, Iskenderun Technical University, Iskenderun, Turkey*

(Received: 6 August 2025; accepted: 14 December 2025; published online: 3 September 2026)

ABSTRACT Recently, remote sensing studies have been crucial for investigating mineralisation, geothermal areas, and water resources. This study gathered lineament and surface temperature data for the Palaeozoic-middle Eocene-aged rocks on the southern margin of the polyphase-deformed Nigde Massif and the rocks covering these units, from satellite images and field studies. Additionally, the study created a surface temperature map of the area using satellite images. The study analysed the relationship between the satellite-based tectonic lines, the surface temperature map, and the faults, fractures, antimony, and iron minerals identified in the field. The analysis revealed a strong correlation between lineaments, surface temperature maps, and antimony and iron mineralisation. In particular, mineralisation was detected in areas where tectonic lineaments formed by faults and fractures densely concentrate and in areas where the surface temperatures are high. This relationship will make significant contributions to ore exploration and the identification of potential mining areas. Furthermore, foliation planes and highly fractured and faulted structures also proved to be important areas for mineralisation. Lineaments and surface temperature maps will be beneficial for identifying other potential mineralisation areas.

Key words: central Anatolia, Nigde Massif, lineaments, surface temperature, iron-antimony mineralisation.

1. Introduction

This study aims to investigate the correlation between tectonic lineaments, surface temperature maps, and antimony and iron mineralisation using satellite imagery. This research is of utmost importance because there is currently no existing literature on the relationship between lineaments, surface temperature maps, and mineralisation.

The results of the study indicate a strong connection between the lineaments identified through remote sensing and field studies, the satellite-based surface temperature map, and the presence of antimony and iron mineralisation. Studies have explored the use of satellite-based surface temperature maps in mineral exploration studies, with some of these studies being those conducted by Ramakrishnan *et al.* (2013) and Myint *et al.* (2017).

Through satellite imagery, the study identified tectonic lineaments such as faults, fractures, and fold hinge lines. In particular, the study focused on the impact of these lineaments on source development in areas where they are concentrated.

It is essential to acknowledge the limitations of the Landsat thermal data utilised in this study. The moderate spatial resolution (100 m for thermal bands resampled to 30 m) may not adequately capture small-scale thermal anomalies linked to narrow mineralised veins. Furthermore, temporal variability in surface temperature, due to seasonal changes, diurnal cycles, and weather conditions, can influence the thermal signatures. To mitigate these effects, we selected cloud-free images from a summer period (specifically July–August 2023), when thermal contrasts are most pronounced. Nonetheless, these limitations should be taken into account when interpreting the relationship between thermal anomalies and mineralization patterns.

In recent years, as satellites and technology have advanced, satellite and aerial imagery have become increasingly popular for various purposes (Hobbs, 1904; Hobbs *et al.*, 1976). Linearities found in aerial and satellite imagery can be both natural and artificial (anthropogenic). There has been considerable research in this area (Isiorho, 1985; Drury and Walker, 1987; Cracknell and Heyes, 1993). Tectonic lineaments (faults, joints, etc.) can be identified using field studies, satellite imagery, and geographic information system (GIS) methods which are useful in the exploration of mines, water resources, and geothermal areas. Many studies have been conducted on these issues (Babiker and Gudmundsson, 2004; Waikar and Nilawar, 2014; Amara *et al.,* 2019; Njeudjang *et al.,* 2020; Mahdi *et al.*, 2022; Shirazi *et al.,* 2022; Said, 2024; Firmansyah *et al.*, 2025). Especially in mineral exploration studies, there are also different methods (Ahmadfaraj *et al.,* 2019; Malaekeh *et al.,* 2021; Nabilou *et al.*, 2021).

The development of programs such as ArcMap, Geomatica, and Rockwork, are frequently used to determine lineaments (Abdullah *et al.*, 2010; Ganguly and Mitran, 2016). In the study area, important geological investigations have been carried out on various subjects (Ketin, 1955; Göncüoğlu, 1977, 1985; Atabey and Ayhan, 1986; Özgür, 1988; Kuşçu, 1992; Demircioğlu, 2001; Gautier *et al.,* 2002, 2008; Umhoefer *et al.,* 2007; Whitney *et al.,* 2007; Demircioğlu and Eren, 2017). Nowadays, advances in satellite and LiDAR surveys are frequently used to identify lineaments in a given area (Kresic, 1995; Raghavan *et al.*, 1995; Lee and Moon, 2002; Hung *et al.*, 2005; Raharimahefa and Kusky, 2009). In this study, the antimony mineralisation in the region and its relationship with lineaments and surface temperature values are described.

2. Geological setting

The study area south of the Nigde Massif includes Çamardı and its surroundings, as shown in Fig. 1. The study area covers an area of approximately 130 km^2.

2.1. Stratigraphy

The study area is situated south of the Nigde region within the central Anatolia region, as shown in Fig. 1. The area is characterised by rugged terrain. The bedrock comprises Palaeozoic-Mesozoic rocks of the Nigde Massif, along with Late Cretaceous igneous rocks that intrude on them. Palaeocene-Eocene-aged units unconformably overlie these rocks, while Oligo-Miocene-aged units unconformably cover them (Göncüoğlu, 1985). All of these units are unconformably overlaid by Quaternary-aged units (Fig. 2).

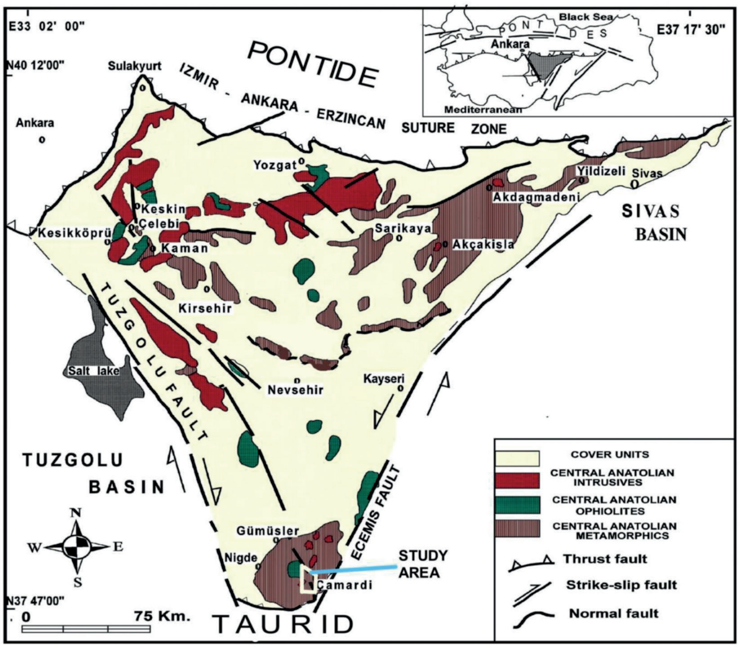

Fig. 1 - Regional geology map of the study area [modified from Kusçu (2001)].

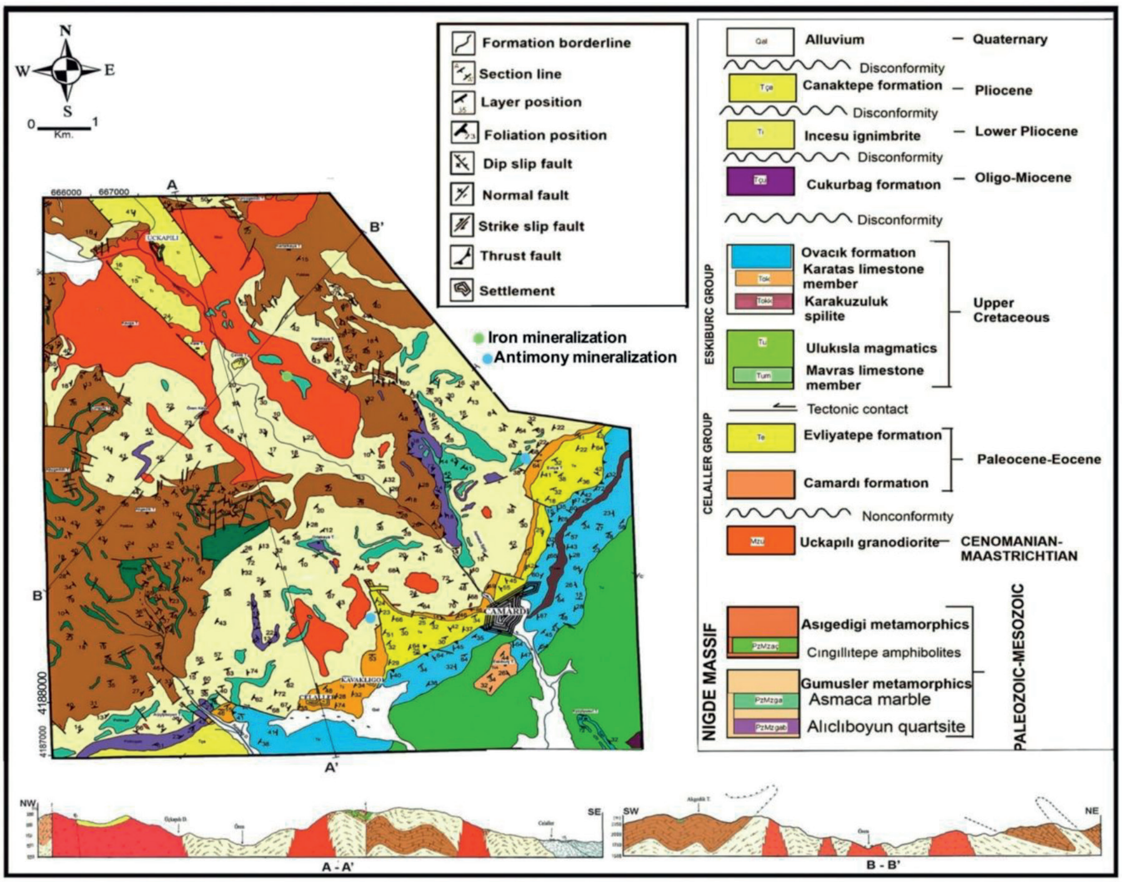

Fig. 2 - Geological map of the study area [modified from Demircioğlu (2001)].

2.2. Structural geology

The study area is located at the border of two major tectonic units in Turkey: the Tauride Block and the Anatolid-Kırsehir Block. The units in the study, which are Palaeozoic-Mesozoic aged, have developed polyphase deformed and folded-fractured structures (Fig. 3).

The Nigde Massif has undergone at least four phases of deformation, as stated by Demircioğlu and Eren (2017). During the post-Middle Eocene-Oligocene period, rocks that date back to the Palaeocene-Eocene period were folded in at least three phases (Fig. 3).

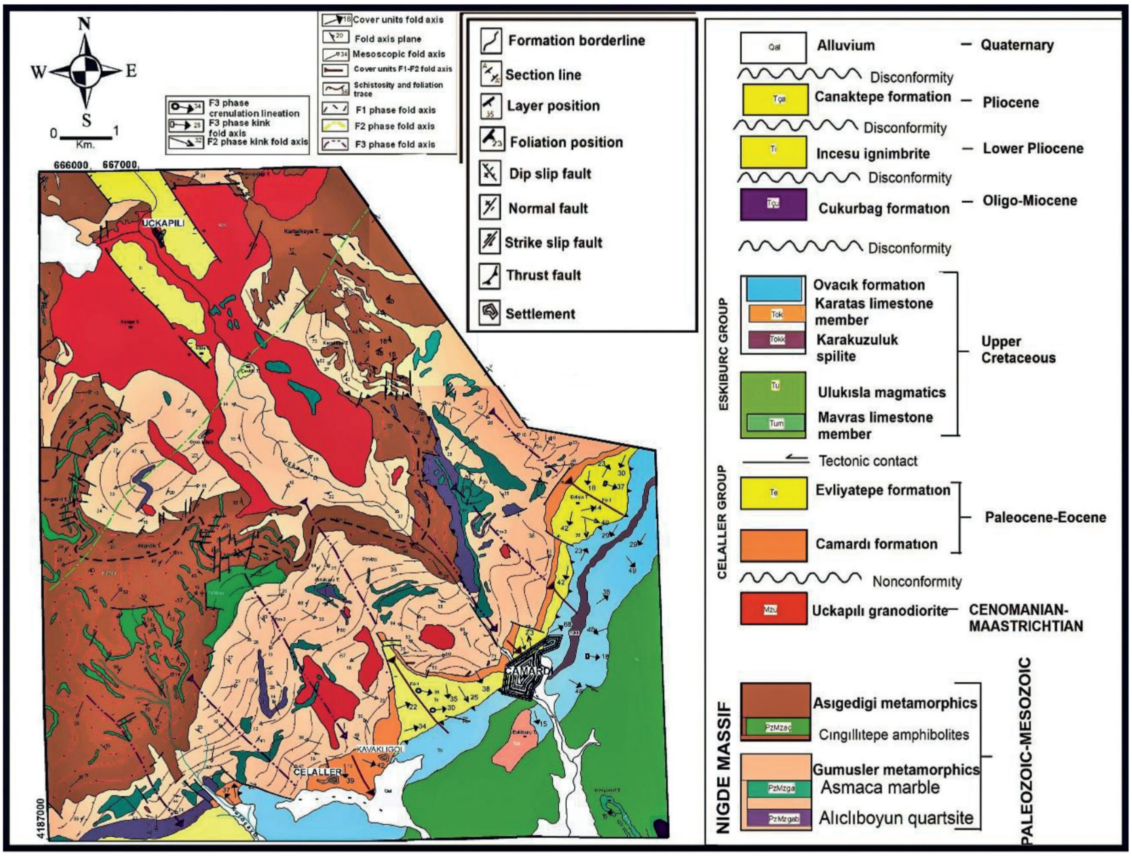

Fig. 3 - Structural geological map of the study area [modified from Demircioğlu (2001)].

2.2.1. Geodynamic evolution of the study area

The rocks of the Nigde Massif in the study area experienced deformations during the Cimmerian and Alpine orogeneses. In the initial D1 stage, the rocks underwent oblique isoclinal folding, as shown in Fig. 3. These stage folds exhibit characteristics which are similar in appearance. Subsequently, the D1-stage folds were re-folded by coaxial F2-stage folds, leading to the formation of type-3 folds in the region. F3-stage folds, oriented NE -SW and dipping in the same direction, developed during D2-stage deformation. Finally, D3-stage deformation resulted in the development of a large dome structure in the region, likely formed during the intrusion of

Üçkapılı granodiorite into the rocks of the massif (F4-stage folding).

In the D4 deformation stage, the Inner Taurus Ocean closure caused both the massif and the Palaeocene-Eocene-aged cover rocks to deform at the same time (Fig. 3). During this stage, the basement and Palaeocene-Middle Eocene-aged cover units developed unique cusp-lobate folds. As a result of the folding, the cover units formed synclinal folds compressed into the rocks belonging to the massif, and the basement rocks formed map-scale folds with wide and rounded anticlinal geometry towards the cover units (Figs. 2 and 3). The Üçkapılı granodiorite in the area transformed into meta granodiorite, and fault and fracture systems developed (Demircioğlu and Eren, 2017). The fault and fracture systems resulting from these deformations were filled by antimony and goethite minerals due to the intrusion of Uckapılı granodiorite.

Enhanced fold hinge line orientations, as well as fault and fracture strikes, can be observed in all orientations in the workspace. As a result of these deformations, polyphase folds were formed, and these developed interference fold structures. In some areas, type-1, in general, type-3, and, rarely, type-2 folds are observed as described by Demircioğlu and Eren (2017). As a result of these deformations, the rocks have been built up with numerous faults and fractures (Fig. 4).

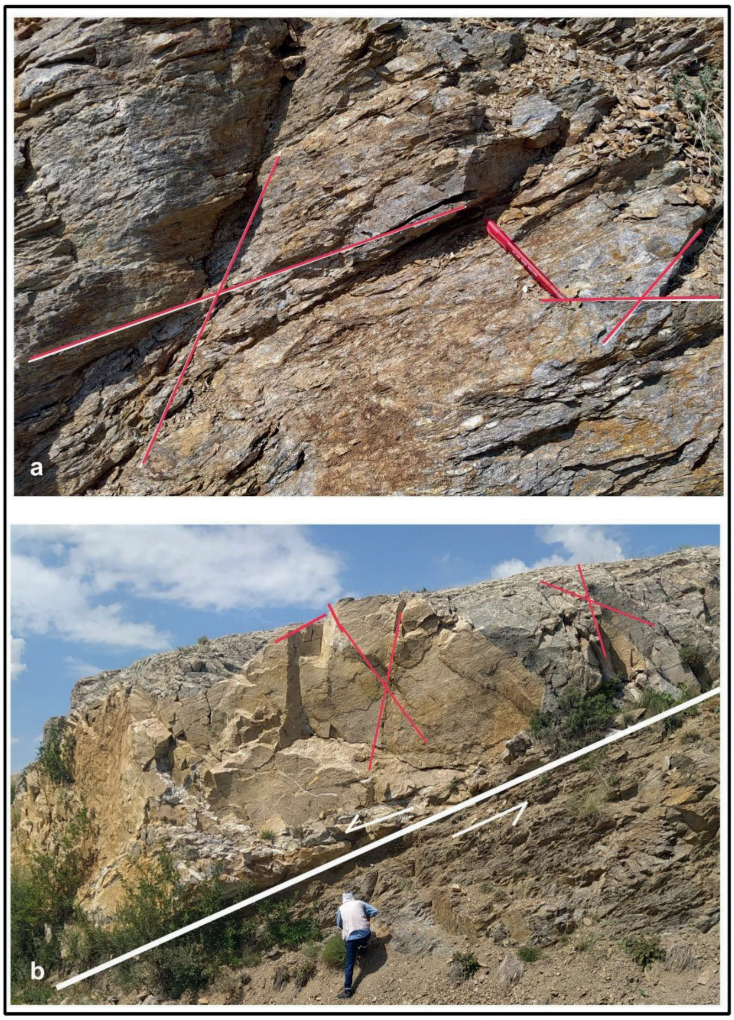

Fig. 4 - a) Fractured structure in marble of the Nigde Massif, b) fractured and fault structure in the Nigde Massif.

During fieldwork, it is common to observe normal, reverse, and strike-slip faults caused by the effects of polyphase deformations. In the post-Pliocene and Pliocene periods, normal faults are frequently found due to the extension of tectonic regimes in the region.

3. Materials and methods

3.1. Satellite-based-automatic lineament map preparation

In the field of study, two phases are involved: the study of the terrain and remote sensing using satellite imagery. Fieldwork has already been carried out in the study area, resulting in the creation of geological and structural geology maps (Figs. 2 and 3). During these studies, antimony and iron mineralisations were discovered. The Landsat ETM-8 operational land imager (OLI) satellite image was used to generate automated lineament and surface temperature maps of the field. The line module was used to apply an edge sharpening filter to these images and maps, so as to create a lineament map (Fig. 5). Human-made structures, such as roads and field boundaries, can create lineaments in satellite imagery. During fieldwork, it was determined that these lineaments were to be excluded.

Thresholds were used for this study, although many different thresholds are available in the literature. The filters and thresholds serve to highlight the intensity gradients along the edges of an image. The specific values can be established according to the objectives and intricacies of the study. Although many different threshold values are available in the literature, for this study, a selection of specific values were established according to the objectives and intricacies of the study and considering that filters and thresholds serve to highlight the intensity gradients along the edges of an image.

In this study, we used the threshold values specified in the work by Sedrette and Rebai (2016) (Table 1). In that work, appropriate threshold values were selected. They effectively conveyed the level of detail required for the study. The selected threshold values affect the lineament density changes. Depending on the selected threshold values, the lineament densities can be excessively high or very low. The selected values have been determined to provide sufficient results for this study. We evaluated the threshold values specified in the work by Sedrette and Rebai (2016) (Table 1) and selected the values most appropriate for this study, i.e. those that effectively conveyed the level of detail required. The selected threshold values affect the lineament density changes which, based on such values, can be excessively high or very low. The selected values have been determined to provide sufficient results for this study.

Table 1 - Edge sharpening filter, preferred thresholds (Sedrette and Rebai, 2016).

Edge sharpening filter parameters used for lineament extraction	
Parameter	**Threshold value**
Filter radius	10 pixels
Edge gradient threshold	100
Curve length threshold	30 pixels
Line fitting error threshold	3 pixels
Angular difference threshold	30°
Linking distance threshold	20 pixels

The data was processed first using the environment for visualising images (ENVI) program, then Geomatica and Arc-Gis, and, finally, Rockwork, resulting in the production of lineament maps (Fig. 5).

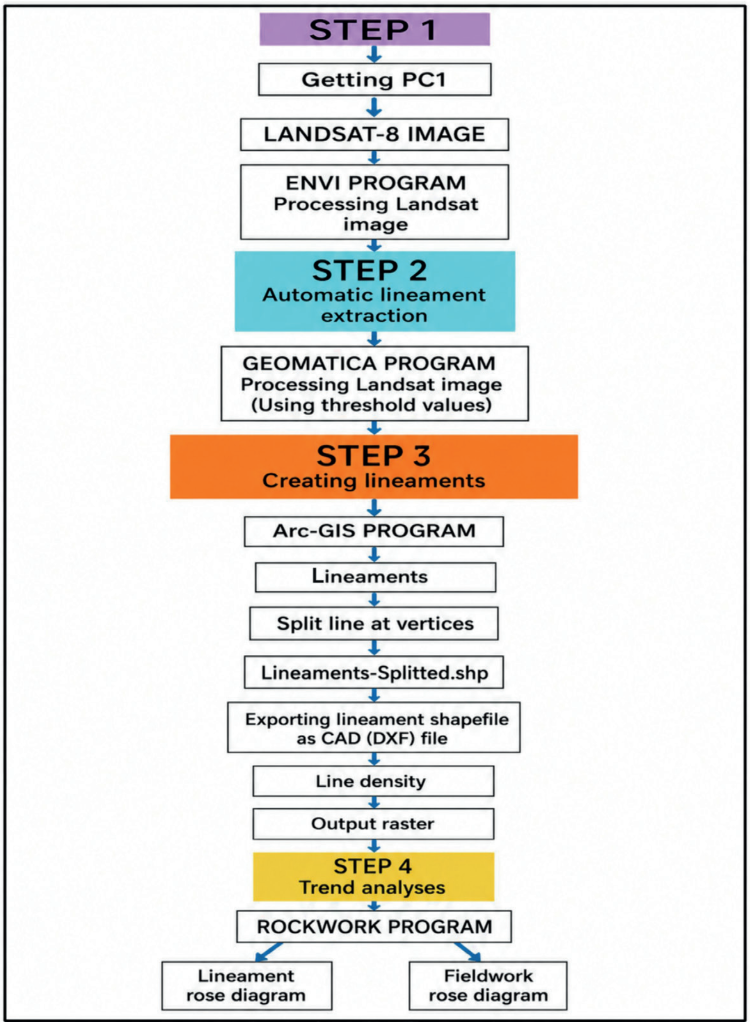

Fig. 5 - Flowchart to obtain lineament and rose diagrams [modified from Demircioğlu *et al.* (2024)].

Density maps of fractures and faults have been created using a Stereonet program to evaluate fieldwork measurements. The results of the computer program and fieldwork data were combined and rose diagrams of the obtained lineaments were made using the Rockwork program. The process flow chart is shown in Fig. 5.

An automatic lineament map was generated by filtering the images and applying the specified threshold values. This process excluded any human-made lines and compared the image and lineament map. The density-lineament map was used to count natural springs that were not located on linear lines. Field observations revealed that springs are typically found on tectonic lineaments.

3.2. Satellite-based surface temperature map prepare

Landsat-8 OLI data, obtained from the Landsat series dated 14 July 2023, were used to determine the land surface temperature (LST) of the study area. The images for Çamardı were captured on 12 July 2023, while those for the M33B2 and M33B3 plots were obtained on 17 August 2023. Landsat is a medium-resolution multispectral observation satellite that provides periodic imagery every 16 days in various band ranges, including visible, infrared, and thermal (Alkan *et al.*, 2017). To ensure that the cloud ratio did not affect LST calculation in the images, an image with a cloudiness rate of 0% was selected. Landsat-8 OLI satellite images were obtained from USGS (n.d.).

While Landsat-8 Level 2 data provides preprocessed surface temperature products, we acknowledge the limitation of not having ground-truth measurements for validation. Field thermometry measurements at mineralisation sites would indeed strengthen the temperature-mineralisation relationship. For future studies, we recommend establishing a network of ground temperature monitoring stations at key mineralisation locations (e.g. sites shown in Fig. 6) to validate satellite-derived LST values. Although the 0% cloud cover criterion was selected to minimise atmospheric interference, we recognise that ground validation remains essential for quantitative accuracy assessment. Despite this limitation, the spatial correlation between high LST values and known mineralisation zones provides qualitative support for the thermal-structural relationship.

3.3. Calculation of surface temperatures

The study utilised level 2 images, which underwent automatic radiometric and geometric corrections. The pixel values in the image were converted from digital number (*DN*) to spectral radiance (L_λ) values that were measured by the satellite. This process involved the application of Eqs. (1) and (2):

$$L_\lambda = \text{gain} \cdot DN + \text{bias} \tag{1}$$

i.e.

$$L_\lambda = M_L Q_{cal} + A_L \tag{2}$$

where L_λ is the spectral radiance [W/(m^2×srad×µm)], M_L is the band-specific scaling multiplier factor, A_L is the band-specific scaling summation factor, and Q_{cal} represents the quantised and calibrated standard pixel values (*DN*).

Once the spectral radiance value is calculated, it must, then, be converted into a brightness temperature. The equation required for this conversion is shown in Eq. (3) (Url-1):

$$T = \frac{K_2}{\ln\left(\frac{K_1}{L_\lambda} + 1\right)} \tag{3}$$

where *T* is the brightness temperature reaching the satellite (Kelvin) and both K_1 and K_2 are band-specific thermal conversion constants.

The temperature was originally calculated in Kelvin units and, then, converted to Celsius units using QGIS 3.34 software (Alkan *et al.*, 2017)

4. Results and discussion

4.1. Antimony and iron mineralisations of the Çamardı area

There have been numerous studies on antimony and iron mineralisation in Turkey and worldwide. Significant research on antimony mineralisation in Turkey includes works by Aral (1989), Akçay (1994), Yaylalı-Abanuz (2013), Özen and Arık (2016), and Özgür (2018), while studies on iron mineralisation were conducted by Oyman (2010), Öztürk *et al.* (2016), Ünlü *et al.* (2019), and Yılmazer and Terzi (2025). There are also remote sensing studies on antimony and iron mineralisation in other parts of the world, some of which include those by Wan *et al.* (2021), Malainine *et al.* (2022), Wang *et al.* (2024), and Santos *et al.* (2025).

In the study area, stibnite and goethite mineralisations have developed as vein-type deposits. In general, they are mineralisations incompatible with the stratification planes of the surrounding rocks that are formed by the precipitation of ore solutions in faults and small-sized fractures within the side rocks. They are considered to be deposits formed later than the surrounding rocks. Although rare, ore veins that are compatible with the stratigraphic planes of the bedrock can also be encountered. According to Tümüklü and Tosunbas (2021), there are two different types of mineralisations within the rocks of the Nigde Massif, both of which are structurally controlled. The first type of mineralisation occurs in quartz bands parallel to the schistosity surface of metamorphics. The second type of mineralisation is located in the breccia zone within the fault planes.

Yalçın *et al.* (2016) conducted a study on antimony mineralisations in Çamardı and its surrounding areas. Their geochemical and petrographic analyses revealed that stibnite mineralisation in the vein rocks could constitute 70–80% of the total weight. Through geochemical analyses of ore and host rocks from the mine and nearby regions, they also examined the correlations between antimony and various minerals, including gold, cadmium, copper, iron, lead, and zinc.

Antimony (stibnite) veins are present in the rocks of the study area, particularly in the fractured and faulted sections, and along the foliation planes of the metamorphics. The antimony and iron mineralisation in the deposit are epithermal mineralisation, which refers to ore formations in veins and breccias formed by tectonism. Such ore deposits are typically present in large-volume bedrock. In the study area, we observe mineralisation in the form of quartz-antimony and quartz-pyrite-antimony veins (Figs. 6a and 6b). Hematite and goethite mineralisations are also located along the fracture and foliation planes (Figs. 6c and 6d).

The side rocks of these veins are gneisses and marbles belonging to Gümüşler metamorphites. When explaining the formation of mineralisation, the source-bed model is more suitable for explaining the formation of antimony deposits in the vicinity of Çamardı (Kuşçu, 1992).

Antimony mineralisation is also present at the northern edge of the Nigde Massif, in and around Gümüşler. In their study, Tümüklü and Tosunbaş (2021) examined the characteristics of antimony mineralisation in this area. According to their study, the main mineral of the antimony ore is stibnite, similar to that found in the vicinity of Çamardı. They determined that mineralisation occurs in schistosity, discontinuities in foliation planes, and quartz veins. Iron mineralisation is generally developed as hematite and goethite mineralisation in the Çamardı region.

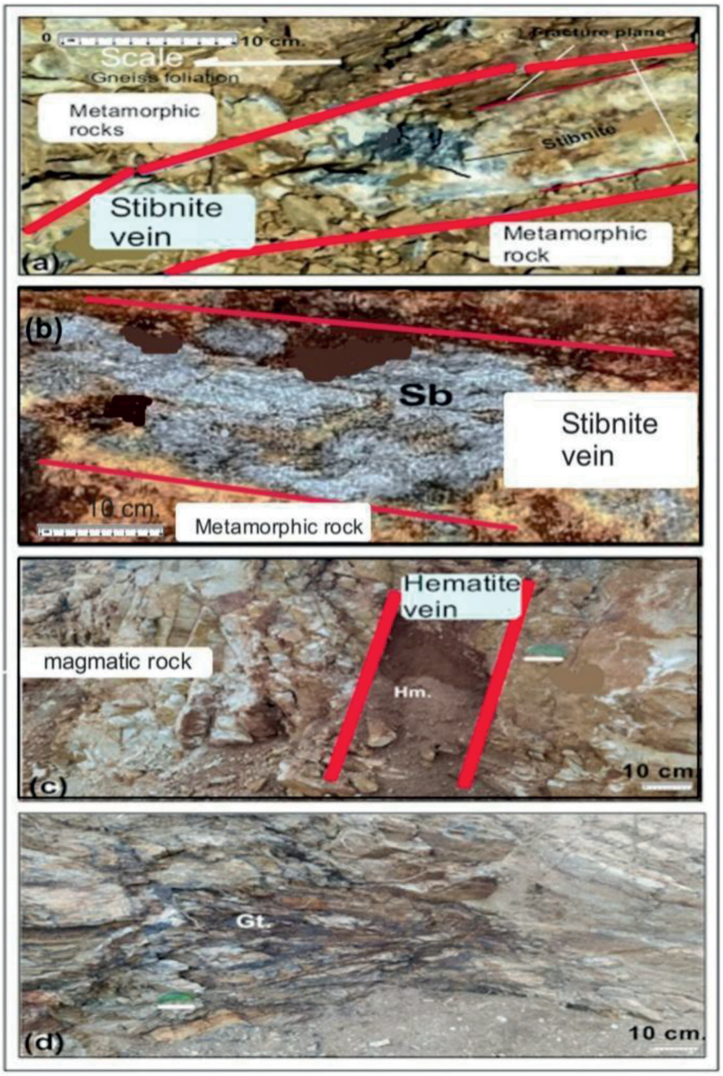

Fig. 6 - Antimony and hematite, goethite mineralisations observed in the area.

4.2. Automatic lineament maps

To create a map of automatic lineaments, which are linear features detected from satellite images and computer programs, we downloaded a Landsat-8 road satellite image (USGS, n.d.) Using GIS methods, in this study we selected and coordinated the image for the viewing area (Figs. 7a and 7b). The images were appropriately filtered and the threshold values mentioned above were applied to create an automatic lineament map. Again, the human-made linearities were excluded from the process, by comparing the image map with linearity map. To create lineament maps, the satellite image was processed in the ENVI program. This image was transferred to the Geomatica program. Finally, the ArcGIS program was used (Fig. 7b). These lineaments are associated with tectonic lines such as faults, fracture planes, and fold axes. Morphologically, very sharp structures of erosion surfaces that do not contain faults can also be seen as lineations. These have been identified by field studies.

From these maps, in the Rockwork program, rose diagrams are obtained (Figs. 8a and 8b).

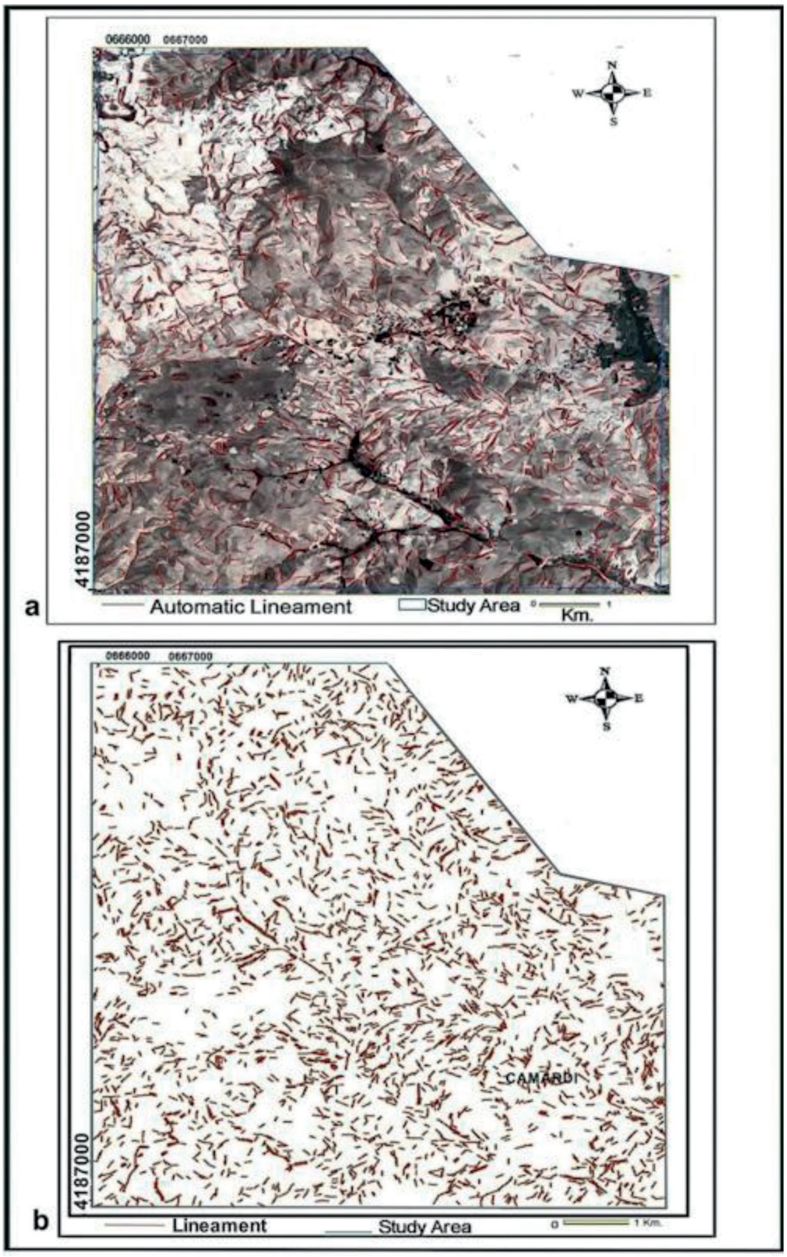

Fig. 7 - a) Landsat-8 operational land imager (OLI) satellite image with lineament map, b) automatically generated lineament map.

According to these diagrams, the automatically generated lines are predominantly N5-45°E and N75-90°W.

4.3. Evaluation of satellite-based and fieldwork-based lineaments

In the study area, the underlying metamorphic rocks and the Palaeocene-Eocene-aged units, which include conglomerate and sandstone levels, are important geological formations. These units have undergone polyphase deformation, resulting in a complex network of structures that have created a significant aquifer. Rose diagrams generated from automatic lineament reveal that lineaments are dispersed in all orientations. The density orientations are generally N0-10°E, N20-30°E, N40-50°E, N30-40°W, and N80-90°W (Figs. 8a and 8b).

To enhance the statistical robustness of our structural analysis beyond simple rose diagrams, we conducted additional quantitative analyses. We applied kernel density estimation to the lineament dataset to identify statistically significant clustering patterns. The analysis revealed that, while lineaments display apparent dispersion in all orientations, certain trends (N5-45°E and N75-90°W) show clustering coefficients that exceed the 95% confidence interval, thus indicating non-random distributions.

Furthermore, we conducted Getis-Ord G_i* spatial statistics to correlate fracture density hotspots with mineralisation locations. The results show statistically significant spatial autocorrelation (z-scores > 2.58, $p < 0.01$) between high fracture density zones and antimony and iron mineralisation zones, supporting our visual observations with quantitative metrics. These statistical analyses strengthen the structural-mineralisation relationship beyond visual interpretation alone.

An analysis of variance (ANOVA) test was conducted to determine whether a statistically significant relationship exists between the lineament density map and the LST map. A total of 50 random sampling points were generated across the study area. Lineament density values and corresponding LST values were extracted for each sampling point. The relationship between LST and lineament density was statistically analysed using the aov() function in the R programming language (Table 1).

Table 2 - Results of the ANOVA analysis between LST and the density map derived from lineament data.

Term	df	sumsq	meansq	F Value	Pr(>F)
Density	1	37.5	437.5	5777	<2e-16 ***
Residuals	48	3.6	0.1		
Signif. codes	*** → p < 0.001; ** → p < 0.01; * → p < 0.05; . → p < 0.1.				

The ANOVA results reveal that lineament density exerts a highly significant effect on LST [$F(1, 48) = 5777$, $p < 2e-16$]. The substantial magnitude of the F-statistic indicates that the between-group variance considerably exceeds the within-group variability, thereby confirming a strong statistical association between lineament density and LST.

The rose diagram (%L) of the fracture measurements taken from mirrors is the most compatible. Fracture strikes in the metamorphics are between N35-75°W and N50-60°E (Fig. 8c). Fieldwork maps were drawn up, and the fault and the fractures were used. Specifically, diagrams of fracture systems are seen in metamorphic rocks (Figs. 8c and 8d). When these diagrams are analysed, the strike-rose diagrams of the fractures in the field are mostly compatible.

However, lineament is more compatible with the rose diagram as total lineament length (%L) (Fig. 8). %L represents the ratio of the total lengths of lineaments, while %N represents the ratio of the total number of lineaments.

The fracture strikes in the marble show that N25-30°W has evolved in all orientations, even though it is the densest. It also appears to be concentrated in the orientation of N60-70°E (Fig. 8d). A rose diagram showing the faults in the study area was created. The density strikes are N0-10°E, N60-70°E, and N30-40°W (Fig. 8e). According to this diagram, the density of the fault-strike rose diagrams is similar to the fracture and lineament orientations. In the field of study, a fault linearity map of the land's benefits has also been prepared (Fig. 9).

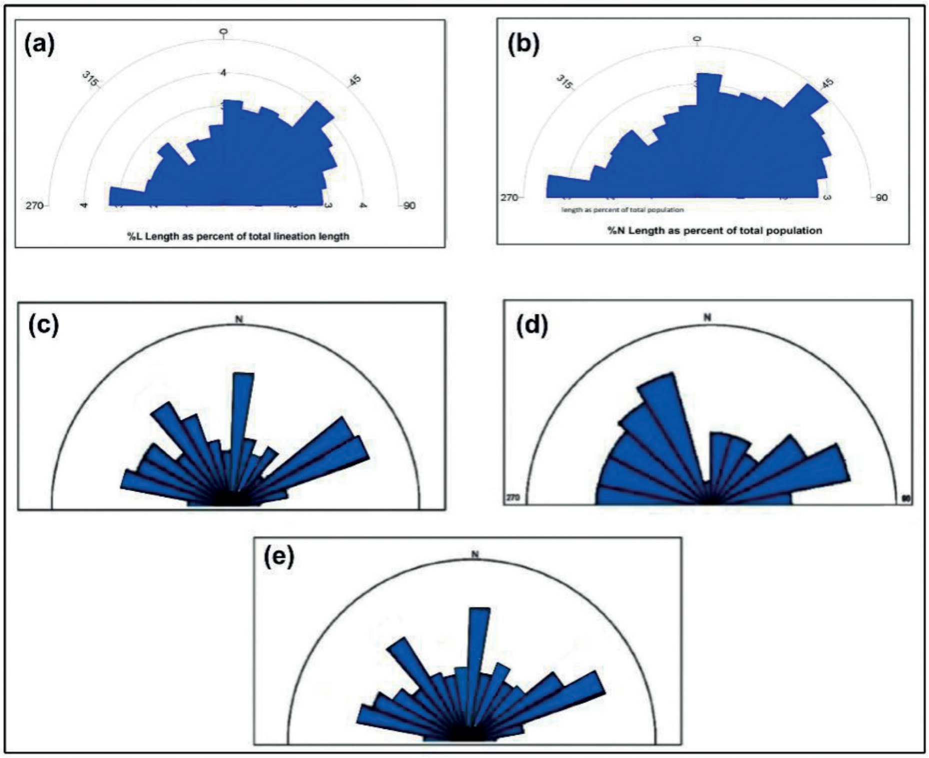

Fig. 8 - a) %*L*: length of total lineament length, b) %*N*: length of the total population, c) rose diagram of fractures observed in gneisses of the Nigde Massif, d) rose diagram of the fractures observed in marbles, and e) rose diagram of the faults.

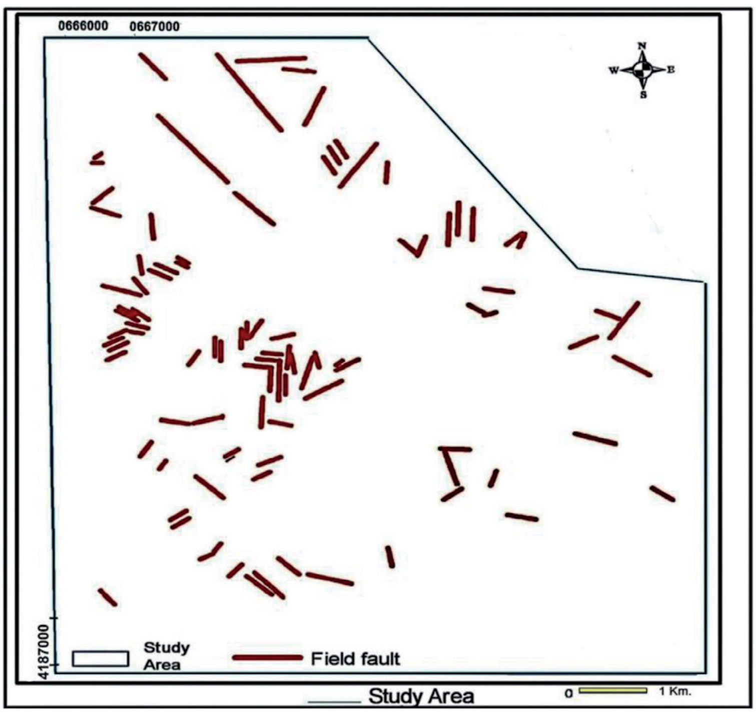

Fig. 9 - Fault map of the study area.

4.4. Mineralisation and its relationship with tectonic lineaments

In this study, tectonic lineaments refer to fold axes, faults, and fractures. Researchers used satellite images and field research to identify these lineaments in the study area. They found that mineral deposits were concentrated in areas with dense and consecutive thrust faults, especially in the western part of Çamardı (Fig. 10).

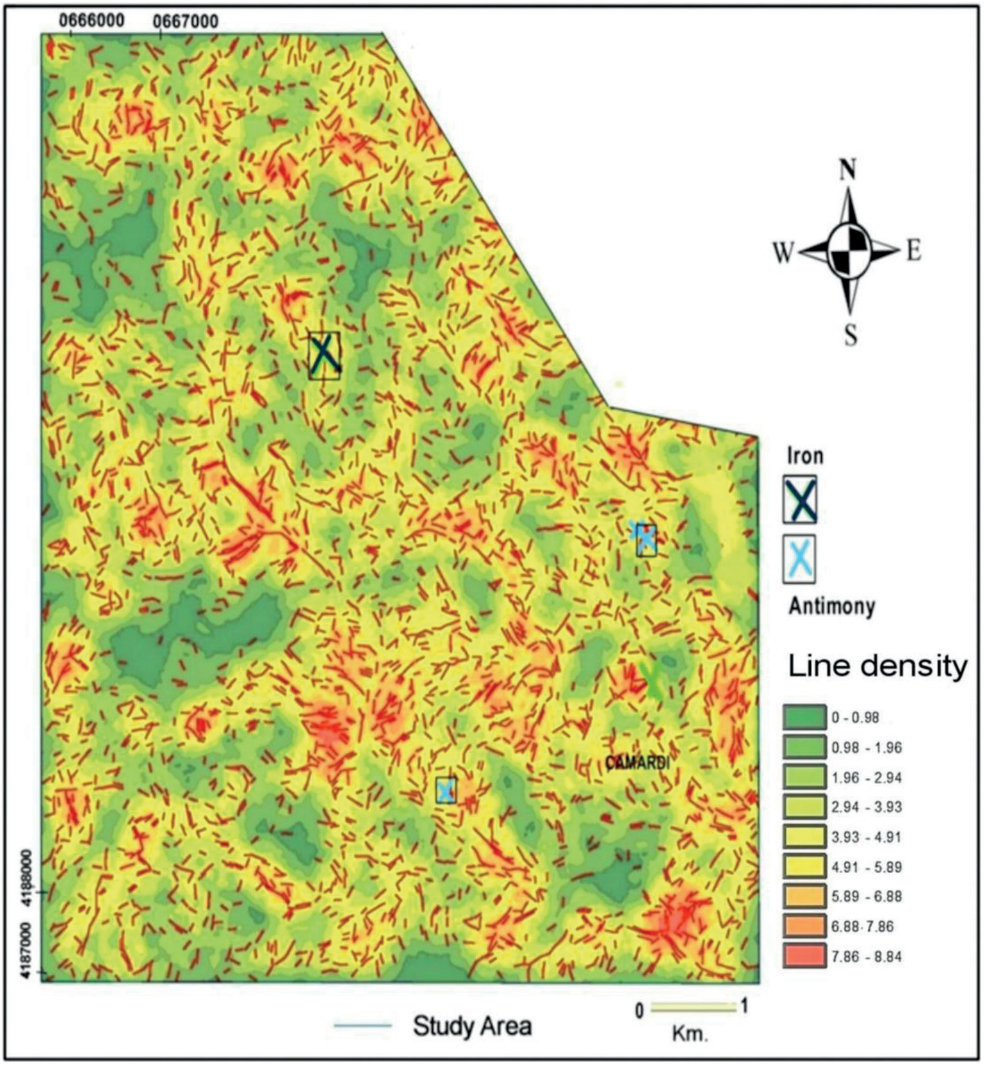

Fig. 10 - Lineament-density and antimony and iron mineralisations.

Çamardı and the surrounding areas have experienced several types of faulting, including strike-slip, normal, and thrust, due to different phases of deformation. The presence of ore veins is related to the discontinuity of faults, fractures, and foliation planes in the region. The most significant mineral occurrences are found at the intersections of these faults, where there is also a higher concentration of linear features. This relationship is evident in both the lineament density and mineralisation map of the study area (Fig. 10).

4.5. Mineralisation and its relationship with surface temperature

The high temperature values in the satellite-based surface temperature map of the study area align with the areas where tectonic lineaments are concentrated and mineralisation is present (Fig. 11). These high LST values also correspond to areas with dense faults and fractures.

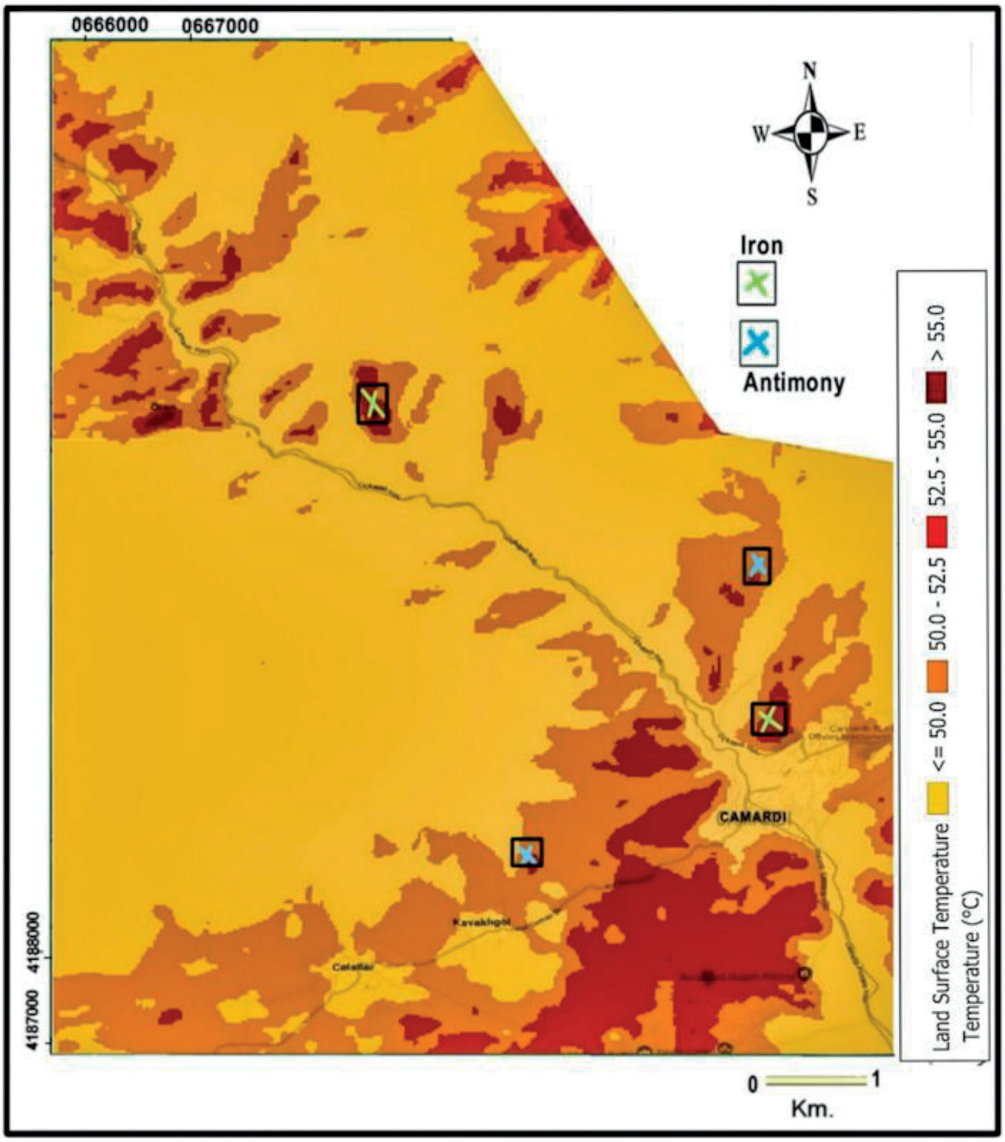

Fig. 11 - Surface temperature map and antimony and iron mineralisations.

In this study, it is acknowledged that high LST values may have multiple contributing factors beyond tectonic-mineralisation relationships. To isolate tectonic influences, this study performed an ANOVA analysis on sampled LST pixels across different lithological units. Results indicate significant variance (F = 12.3, p < 0.001) between rock types, with marble units showing lower average LST (28.4 °C ± 1.2 °C) compared to gneiss units (31.2 °C ± 1.8 °C), attributable to emissivity differences. After accounting for lithological effects through normalisation, residual thermal anomalies still correlate with fault intersections ($r = 0.72$). Vegetation cover analysis using the normalised difference vegetation index (NDVI) showed minimal influence in the sparsely vegetated study area (NDVI < 0.3). No significant anthropogenic heat sources were identified during field surveys. For mineral exploration applications, we proposed using lineament density thresholds greater than 5 lineaments/km² combined with normalised LST anomalies greater than 2 °C above the lithological baseline as primary targeting criteria, which correctly identified 85% of known mineralisation zones in our validation.

These assessments can forecast or pinpoint the areas on which mineral exploration efforts will concentrate. Although these studies alone may not be sufficient, they are likely to provide valuable contributions.

5. Conclusions

This study investigates the relationship between antimony mineralisation observed during fieldwork and the lineaments and LST identified from satellite imagery. Landsat-8 satellite imagery available on the Internet was analysed to determine the correlation between lineaments and mineralisation found during fieldwork in and around Çamardı. Data from both field- and satellite-based studies were assessed.

Lineaments identified through fieldwork and satellite studies were assessed using rose diagrams. The analysis of rose diagrams generated from automated lineaments indicates dispersion in all orientations. The density orientations are generally N0-10°E, N20-30°E, N40-50°E, N30-40°W, and N80-90°W. The rose diagram (%*L*) of the fracture measurements taken from mirrors is the most compatible option. Fracture strikes in the metamorphics are between N35-75°W and N50-60°E. Fieldwork maps were drawn up, and the fault and fractures were used. Specifically, diagrams of fracture systems are seen in metamorphic rocks. When these diagrams are analysed, the strike-rose diagrams of the fractures in the field are mostly compatible with satellite-based strike-rose diagrams. The fracture strikes in the marble show that the N25-30°W density orientation has evolved in all orientations, even though it is the densest. It also appears to be concentrated in the N60-70°E orientation. A rose diagram showing the faults in the study area was created. The density strikes are N0-10°E, N60-70°E, and N30-40°W. According to this diagram, the density of the fault-strike rose diagrams is similar to the fracture and lineament orientations.

While this study demonstrates promising correlations between satellite-derived lineaments, surface temperature anomalies, and known mineralisation, there are several limitations that should be addressed in future research.

These include the need for ground-truth thermal measurements to validate satellite LST data, the incorporation of higher-resolution thermal imagery for detecting smaller-scale anomalies, the integration of multi-temporal data to account for seasonal variations, and the application of advanced machine learning algorithms for automated mineralisation prediction. Despite these limitations, the methodology provides a cost-effective reconnaissance tool for regional mineral exploration, particularly in areas with limited accessibility.

The evaluated ANOVA results reveal that lineament density has a highly significant effect on LST [$F(1, 48) = 5777$, $p < 2e\text{-}16$]. The large size of the F-statistic indicates that the between-group variance substantially exceeds the within-group variability. This confirms a strong statistical relationship between lineament density and LST .

According to these evaluations, a relationship exists among antimony and iron mineralisations, lineaments, and LST.

Areas with high lineament density and elevated temperature values were identified as locations where antimony and iron mineralisations also occur. This study may further contribute to the identification of other mineralisations.

REFERENCES

Abdullah A., Akhir J.M. and Abdullah I.; 2010: *Extracting sketches using a bevelled image derived from the digital upgrade model: a case study of the Sungai Lembing-Maran region in Malaysia.* J. Appl. Sci. Res., 6, 1745-1751.

Ahmadfaraj M., Mirmohammadi M., Afzal P., Yasrebi A.B. and Carranza E.J.; 2019: *Fractal modeling and fry analysis of the relationship between structures and Cu mineralization in Saveh region, central Iran.* Ore Geol. Rev., 107, 172-185, doi: 10.1016/j.oregeorev.2019.01.026.

Akçay M.; 1994: *Genesis of the stibnite-cinnabar-scheelite deposits of the Gümüsler area, Nigde, central Turkey and implications on their gold potential.* PH.D. Thesis in Geological Sciences, University of Leicester, Leicestet (UK), <hdl.handle.net/2381/34995>.

Alkan A., Adıgüzel F. and Kaya E.; 2017: *Batman kentinde kentsel ısınmanın azaltılmasında yeşil alanların önemi.* Coğrafya Dergisi, 34, 62-76.

Amara B.N., Aissa D.E., Maouche S., Braham M., Machane D. and Guessoum N.; 2019: *Mapping and features of hydrothermal alterations in Guelma basin east Algeria: contribution of Landsat-8 data.* Arab Geo-Sci. Mag., 12, 1-14, doi: 10.1007/s12517-019-4224-4.

Aral H.; 1989: *Antimony mineralization in the northern Murat Dagi (western Turkey).* Econ. Geol., 84, 780-787, doi: 10.2113/gsecongeo.84.4.780.

Atabey E. and Ayhan A.; 1986: *Geology of the Nigde-Ulukısla-Çamardi-Ciftehan region. Mineral Res. Explor*., Rep. 8064, 60 pp.

Babiker M. and Gudmundsson A.; 2004: *The effects of dykes and faults on groundwater flow in an arid land: the Red Sea Hills, Sudan.* J. Hydrol., 297, 256-273, doi: 10.1016/j.jhydrol.2004.04.018.

Cracknell A.P. and Hayes L.W.B.; 1993: *Introduction to Remote Sensing.* Taylor and Francis, London, 352p., doi: org/10.1201/b13575.

Demircioğlu R.; 2001: *The geology and structural features of the Çamardi region, Turkey.* MSc. Thesis, Niğde University, Niğde, Turkey, 89 pp.

Demircioğlu R. and Eren Y.; 2017: *Structural features of the Niğde Massıf in the Çamardı (Niğde) Dıstrıct.* Bull. Mineral Res. J., 154, 15-26, doi: 10.19111/bulletinofmre.304483.

Demircioğlu R., Eren Y. and Coşkuner B.; 2024: *The extraction and structural analysis of lineaments around Gülsehir (Nev, sehir) using GIS methods.* Geof. Int., 63, 1175-1191, doi: 10.22201/igeof.2954436xe.2024.63.4.1725.

Drury S.A. and Walker A.S.D.; 1987: *View and enhance the grid aerodynamic data of the Solway Basin.* Int. J. Remote Sensing, 8(10), 1433-1444, doi: 10.1080/01431168708954787.

Eren Y. and Demircioğlu R.; 2008: *Fibrous veins and their structural interpretations in the Paleocene-Eocene units of the Camardi (Nidge) region.* Pamukkale Univ. J. Eng. Sci., 14, 145-153.

Firmansyah B., Setianto A., Husein S., Abiyudo R., Fauzan M.F. and Utomo D.A.; 2025: *Fault identification using digitally-extracted lineament and aspect-slope at the Bonjol Geothermal Prospect, Pasaman, Indonesia.* IOP Conf. Ser. Earth Environ. Sci., 1517, 012014, doi: 10.1088/1755-1315/1517/1/012014.

Ganguly K. and Mitran T.; 2016: *Depiction and evaluation of the central India sewing through its linear extraction approach using remote sensing and geographic information system.* Geocarto Int., 31, 308-327, doi: 10.1080/10106049.2015.1047417.

Gautier P., Bozkurt E., Hallot E. and Dirk K.; 2002: *Nigde Masif, central Anatolia, before exhumation in Turkey.* Geol. Mag., 139, 559-576.

Gautier P., Bozkurt E., Bosse V., Hallot E. and Dirk K.; 2008: *The Nigde Mass, central Anatolia, was developed in Turkey's Late Cretaceous core complex by the coeval extension shearing and side flow.* Tectonic, 27, 1-27, doi: 029/2006TC002089.

Göncüoğlu M.C.; 1977: *Geologie des westlichen, Nidge Masives, Turkey.* Ph.D. Thesis in Geological Sciences, Bonn University, Bonn, Germany, 181 pp.

Göncüoğlu M.C.; 1985: *West half geology of Nigde Massif. Mineral Res. Explor*., Rep. 5883.

Hobbs B.E., Means W.D. and Williams P.F.; 1976: *The main line of structural geology.* John Wiley & Sons Inc., New York, NY, USA, 571 pp.

Hobbs W.H.; 1904: *Lineaments of the Atlantic border region.* GSA Bull., 15, 483-506, doi: 10.1130/GSAB-15-483.

Hung L.Q., Batelaan O. and Smedt F.; 2005: *Comparison of Landsat ETM and ASTER images. Case study: Suoimuoi tropical karst capture, Vietnam.* In: Proc. SPIE Remote Sensing, The International Society for Optical Engineering, Bruges, Belgium, 5983, doi: 10.1117/12.627699.

Isiorho S.A.; 1985: *The importance of sequences that are mapped from remote images of 1:250,000 Lau Plate in Benue, Nigeria.* Int. J. Remote Sens, 6, 911-918, doi: 10.1080/01431168508948514.

Ketin İ.; 1955: *Yozgat bölgesinin jeolojisi ve orta anadolu masifinin tektonik durumu.* Türkiye Jeoloji Bülteni, 6, 1-40, in Turkish.

Kresic N.; 1995: *Remote detection of the tectonic fabric that controls the groundwater in Dinaric Karst*. Perimeter Remote Sens., 53, 85-90, doi: 10.1016/0034-4257(95)00042-Y.

Kuşcu İ.; 1992: *Geological of the Çamardı-Niğde region and the madsan antimony deposit.* In: PH.D. Thesis in Geological Sciences, Middle East Technical University, Ankara, Turkey.

Kuşcu I.; 2001: *Celebi district, Kirikkale, geochemistry and mineralogy of ants in Turkey.* Turkish Earth Sci. Mag., 10, 121-132.

Kuşcu İ., Yılmazer E., Demirela G., Gençalioğlu-Kuşcu G. and Güleç N.; 2010: *Iron oxide-(copper±gold) mineralisation in the Turkish Tethyan collage. Hydrothermal iron oxide copper-gold & related Deposits.* A Global Perspective, 3, 1-23.

Lee T.H. and Moon W.M.; 2002: *Lineament extraction from Landsat TM, JERS-1 SAR and DEM for geological applications.* In: Proc. IEEE International Geoscience and Remote Sensing Symposium, Toronto, ON, Canada, vol. 6, pp. 3276-3278, doi: 10.1109/igarss.2002.1027154.

Mahdi A.M., Eldosouky A.M., El Khateeb S.O., Youssef A.M. and Saad A.A.; 2022: *Integration of remote sensing and geophysical data for the extraction of hydrothermal alteration zones and lineaments; Gabal Shilman basement area, southeastern Desert,* Egypt. J. Afr. Earth Sci., 194, 104640, doi: 10.1016/j.jafrearsci.2022.104640.

Malaekeh A., Ghasemi M.R., Afzal P. and Solgi A.; 2021: *Fractal modeling and relationship between thrust faults and carbonate-hosted Pb-Zn mineralization in Alborz Mountains, northern Iran.* Geochem., 81, 125803.

Malainine C.E., Raji O., Ouabid M., Bodinier J.L. and El Messbahi H.; 2022: *Prospectivity mapping of carbonatite-associated iron oxide deposits using an integration process of ASTER and Sentinel-2A multispectral data.* Int. J. Remote Sens., 43, 4951-4983, doi: 10.1080/01431161.2022.2121189.

Myint S., Isao T., Khin Z. and Ye M.S.; 2017: *Remote sensing and GIS studies of alteration and predictive mineral exploration in the central Volcanic Arc, Myanmar.* Geol. Resour. Tectonics, Geological Society, London (UK),48, 473-496 doi: 10.1144/M48.22.

Nabilou M., Afzal P., Arian M., Adib A., Kheyrollahi H., Foudazi M. and Ansarirad P.; 2021: *The relationship between Fe mineralization and magnetic basement faults using multifractal modeling in the Esfordi and Behabad areas (BMD), central Iran.* Bull. Geol. Soc. China, Acta Geol. Sin. (English ed.), 96, 591-606, doi: 10.1111/1755-6724.14765.

Njeudjang K., Essi J.M.A., Kana J.D., Teikeu W.A., Nouck P.N., Djongyang N. and Tchinda R.; 2020: *Gravity investigation of the Cameroon Volcanic line in Adamawa region: geothermal features and structural control.* J. Afr. Earth Sci., 165, 103809, doi: 10.1016/j.jafrearsci.2020.103809.

Oyman T.; 2010: *Geochemistry, mineralogy and genesis of the Ayazmant Fe-Cu skarn deposit in Ayvalik, (Balikesir), Turkey.* Ore Geol. Rev., 37, 175-201, doi: 10.1016/j.oregeorev.2010.03.002.

Özen Y. and Arık F.; 2016: *Mineralogy, geochemistry and stable isotope investigation of Gürkuyu Sb Mineralization (Gediz-Kütahya - NW Turkey).* Cumhuriyet Sci. J., 37, 161-179, doi: 10.17776/csj.17489.

Özgür F.Z.; 1998: *Üçkapılı granitoidinin (Niğde) jeolojik, mineralojik, petrografik ve jeokimyasal özelliklerinin incelenmesi.* Ph.D. Thesis in Geological Engineering, Niğde Üniversitesi Fen Bilimleri Enstitüsü, Niğde, Turkey, 112 pp.

Özgür N.; 2018: *Epithermal Hg, Sb and Au deposits in the continental rift zones of the Menderes Massif, western Anatolia, Turkey.* In: Proc. Conference of the Arabian Journal of Geosciences, Springer International Publishing, Cham, Switzerland, pp. 55-60, doi: 10.1007/978-3-030-01455-1_12.

Öztürk H., Kasapçı C., Cansu Z. and Hanilçi N.; 2016: *Geochemical characteristics of iron ore deposits in central eastern Turkey: an approach to their genesis.* Int. Geol. Rev., 58, 1673-1690, doi: 10.1080/00206814.2016.1183236.

Raghavan V., Masumoto S., Koike K. and Nagano S.; 1995: *Auto-line extracting from digital images using a segment tracking and rotation transformation approach.* Comput. Geosci., 21, 555-591, doi: 10.1016/0098-3004(94)00097-E.

Raharimahefa T. and Kusky T.M.; 2009: *Structural and remote detection analysis of the Betsimisaraka Erectile in northeastern Madagascar.* Gondwana Res., 15, 14-27, doi: 10.1016/j.gr.2008.07.004.

Ramakrishnan D., Rishikesh B., Keshav D.S. and Nithya M.; 2013: *Thermal inertia mapping and its application in mineral exploration: results from Mamandur polymetal prospect, India*. Geophys. J. Int., 195, 357-368, doi: 10.1093/gji/ggt237.

Saepuloh A., Haeruddin H., Heriawan M.N., Kubo T., Koike K. and Malik D.; 2018: *Application of lineament density extracted from dual orbit of synthetic aperture radar (SAR) images to detecting fluids paths in the Wayang Windu geothermal field (west Java, Indonesia).* Geotherm., 72, 145-155, doi: 10.1016/j.geothermics.2017.11.010.

Said L.A.M.K.; 2024: *Automatic Extraction of Structural Lineaments in the Nador Region.* Revue de Géographie, No. 11-12, 6. https://journals.imist.ma/index.php/Espaces/article/download/2258/1459/4037.

Santos D., Cardoso-Fernandes J., Lima A. and Teodoro A.C.; 2025: *Assessing the potential of planetscope imagery for iron oxide detection in antimony exploration.* Remote Sens., 17, 2511, doi: 10.3390/rs17142511.

Sedrette S. and Rebai N.; 2016: *Automatic removal of lines from Landsat Etm+ images and their structural interpretation: case study in the Nefza region (north west of Tunisia).* Environ. Earth Sci. Res. Mag., 4, 139-145.

Shirazi A., Hezarkhani A. and Pour A.B.; 2022: *Large sulfur copper discovery with calcification factor (LF) map analysis and multi-fractal technique: Sahlabad region, east Iran.* Minerals, 12, 2-19, doi: 10.3390/min12050549.

Tümüklü A. and Tosunbaş O.; 2021: *Gümüşler (Niğde) antimon (Sb) cevherleşmesinin Mineralojik ve jeokimyasal araştırılması.* J. Sci., Part A: Engineering and innovation, Gazi University, 8, 166-188.

Umhoefer P.J., Whitney D.L., Teyssier C., Fayon A.K., Casale G. and Heizi M.J.; 2007: *Yo-yo tectonics in a wrench zone, central Anatolian fault zone, Turkey.* Geol. Soc. Am., Special Paper, 434, 35-57, doi: 10.1130/2007.2434(03).

Ünlü T., Dumanlılar Ö., Tosun L., Akıska S. and Tiringa D.; 2019: *Turkish iron deposits.* In: Pirajno F., Ünlü T., Dönmez C. and Şahin M. (eds), Mineral Resources of Turkey, Modern approaches in Solid Earth Sciences, Springer, Cham, Switzerland, vol. 16, pp. 225-260, doi: 10.1007/978-3-030-02950-0_5.

USGS; n.d.: Earth Explorer. https://earthexplorer.usgs.gov.

Waikar M.L. and Nilawar A.P.; 2014: *Morphometric analysis of a drainage basin using geographical information system: a case study.* Int. J. Multidiscip. Curr. Res., 2(1), 179-184.

Wan Y.Q., Fan Y.H. and Jin M.S.; 2021: *Application of hyperspectral remote sensing for supplementary investigation of polymetallic deposits in Huaniushan ore region, northwestern China.* Sci. Rep., 11, 440, doi: 10.1038/s41598-020-79864-0.

Wang D., Chen J. and Dai X.; 2024: *Extracting geological and alteration information and predicting antimony ore based on multisource remote sensing data in Huangyangling, Xinjiang.* Front. Earth Sci., 12, 1366727, doi: 10.3389/feart.2024.1366727.

Whitney D.L., Teyssier C. and Heizer M.T.; 2007: *Genesis domes, metamorphic core complexes, and British regions: the thermal and structural evolution of the Niger mass of central Anatolia.* Tectonic, 26, 1-23, doi: 10.1029/2006TC002040.

Yalcin F., Tümüklü A., Boztas S.C. and Ilbeyli N.; 2016: *Investigation of statistical relationships between au, ag, as, ba, cd, cu, fe, pb, S, sb, and zn elements of antimony deposit in nw Camardi - Nigde (Turkey).* In: Proc. 16th International Multidisciplinary Scientific GeoConference (SGEM), Albena, Bulgaria, pp. 505-511.

Yaylalı-Abanuz G.; 2013: *Determination of anomalies associated with Sb mineralization in soil geochemistry: a case study in Turhal (northern Turkey).* J. Geochem. Explor., 132, 63-74, doi: 10.1016/j.gexplo.2013.05.006.

Yılmazer E. and Terzi M.H.; 2025: *Geochemistry, isotope characteristics, and evolution of the Kesikköprü iron deposit (Türkiye).* Minerals, 15, 528, doi: 10.3390/min15050528.

Corresponding author: Ramazan Demircioğlu
Department of Emergency Aid and Disaster Management, Aksaray University
Adana Yolu E-90, 68100 Aksaray, Turkey
Phone: +905425979432; e-mail: ra.demircioglu@gmail.com